Appendix E

Supplementary Information for Chapter 6: Development of tools to calculate ion mobility at arbitrary field strengths

This appendix contains the supporting information for Chapter 6, and is analogous to the supporting information to the following manuscript:

> Haack, A.,* Ieritano, C.,* Hopkins, W. S. MobCal-MPI 2.0: An Accurate and Parallelized Package for Calculating Field-Dependent Collision Cross Sections and Ion Mobilities. *Analyst.* **2023**, 148, 3257 – 3273. *Equal contribution.
>
> https://pubs.rsc.org/en/content/articlelanding/2023/AN/D3AN00545C

*Equal contribution.

Table of Contents

Supplementary Sections

Section S6-1: A brief review of other CCS calculation tools

1. In the mid-1990s, the MobCal program[1,2] was published for CCSs in helium, which is, arguably, the most famous CCS predictor. It allows for three different types of CCS calculations: (1) the Projection Approximation (PA), in which the "shadow" of the ion is averaged over all orientations, (2) the Exact Hard Sphere Scattering (EHSS) model, which actually calculates collision trajectories of the ion-neutral pair but treats their interaction with a hard-sphere potential, and (3) the Trajectory Method (TM), which is similar to the EHSS model but uses a more realistic Lennard-Jones (LJ) 12-6 potential. As these methods increase in accuracy (from PA to TM), their computational cost also increases. The MobCal code was later expanded to N_2 as collision gas[3,4] and further updates to the interaction potential were undertaken, specifically accounting for the polarizability of N_2 and its quadrupole moment.[5,6] Recently, further updates to the interaction potential and parallelization of the code, now termed MobCal-MPI, increased accuracy and especially speed of the calculations.[7,8]
2. A lesser common known variant of the MobCal code is the HPCCS program,[9] which also utilizes the TM and can compute CCSs in He and N_2.
3. The IMoS code[10–12] became also quite popular in recent years. In contrast to MobCal, IMoS explicitly calculates the drag inflicted on the ion through the bath gas. This is done by a trajectory method (with realistic interaction potentials), where the velocity of both the ion and bath gas are explicitly considered. This is in contrast to MobCal where the relative velocity of the ion-neutral pair is considered. Despite the different mathematical approach as compared to MobCal, it has been shown that both methods perform equally well.[13] IMoS then obtains the ion mobility coefficient, K, from the calculated drag and the CCS through rearranging Eq. (4) of the main manuscript.
4. Collidoscope[14] is yet another CCS predicter utilizing the TM and a LJ 12-6 interaction potential including polarizability for both He and N_2 as collision gases. Its accuracy was reported to be similar to IMoS. Parallelization of the code makes it similar fast to MobCal-MPI, HPCCS and IMoS.

5. Large ions (proteins, supramolecular complexes, *etc.*) make the usage of the TM both computationally infeasible but also unnecessary. Because of their size, the fine details of the scattering process become less important and projection approximation algorithms provide sufficiently accurate results. A prominent example is the PSA method.[15–18] Through careful calibration of the collision probabilities, even temperature dependencies of the CCS are reproduced.

Section S6-2: Collision dynamics

The amount of momentum transferred upon a collision between two particles (at relative velocity g, impact parameter b and assuming a spherically symmetric interaction potential), can be calculated from the scattering angle, χ, and is proportional to $1 - \cos\chi$. In Figure S6-1, some example trajectories are shown for two different relative velocities and a set of impact parameters (ranging from $b = 0$ to a cut-off value b_{max}). It further shows the amount of momentum being transferred as a function of the impact parameter. The integral under these curves is proportional to the momentum transfer cross section, $Q^{(1)}(g)$. We can separate collision events into two categories: glancing collisions (large b, only probing the attractive part of the potential) and striking collisions (small b, probing both the attractive and repulsive part of the potential). Both kinds contribute to the overall momentum transfer for small velocities but as can be seen in Figure S6-1, for higher relative velocities, only the striking collisions transfer momentum. At higher velocities, trajectories with large b do not significantly contribute to the total momentum transfer.

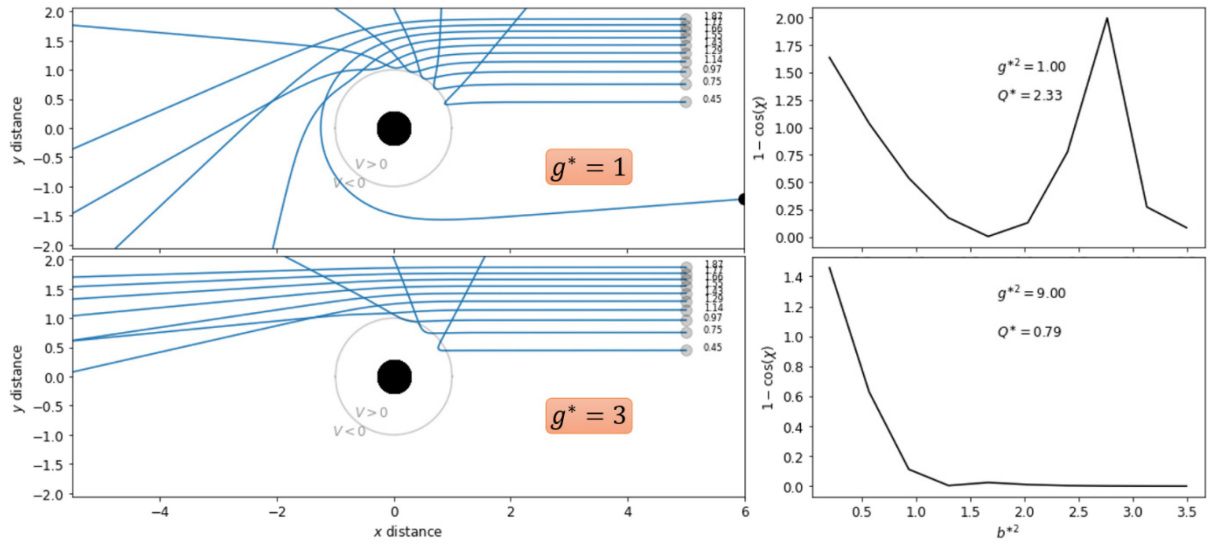

Figure S6-1. Left: Collision trajectories for two different relative speeds, g^*, and for a set of impact parameters, b^* (in dimensionless units). **Right**: Corresponding momentum transfer as a function of b^{*2}. The interaction potential is assumed to be spherically symmetric and the grey circle denotes the distance at which the potential becomes repulsive.

Thus, when integrating over both the velocity as well as impact parameter space, using a common upper limit, b_{max}, will result in a lot of trajectories that do not contribute to the overall momentum transfer integrals. This can be seen even better in Figure S6-2, which shows the momentum transfer as contour plot over both velocity and impact parameter space. As can be seen, most trajectories (started at pairs of (b, g)) would yield close to zero momentum transfer and can thus be neglected to save computing time. Consequently, it is beneficial to calculate a b_{max} value for each velocity grid point. This was already done in the original MobCal implementation, the strategy for which is retained in MobCal-MPI 2.0. This is depicted with the red line in Figure S6-2. This way, at every of the *inp* velocity points, *imp* impact parameter (and orientation) samples are taken, but only for $b \leq b_{max}(g)$, where there is significant momentum transfer.

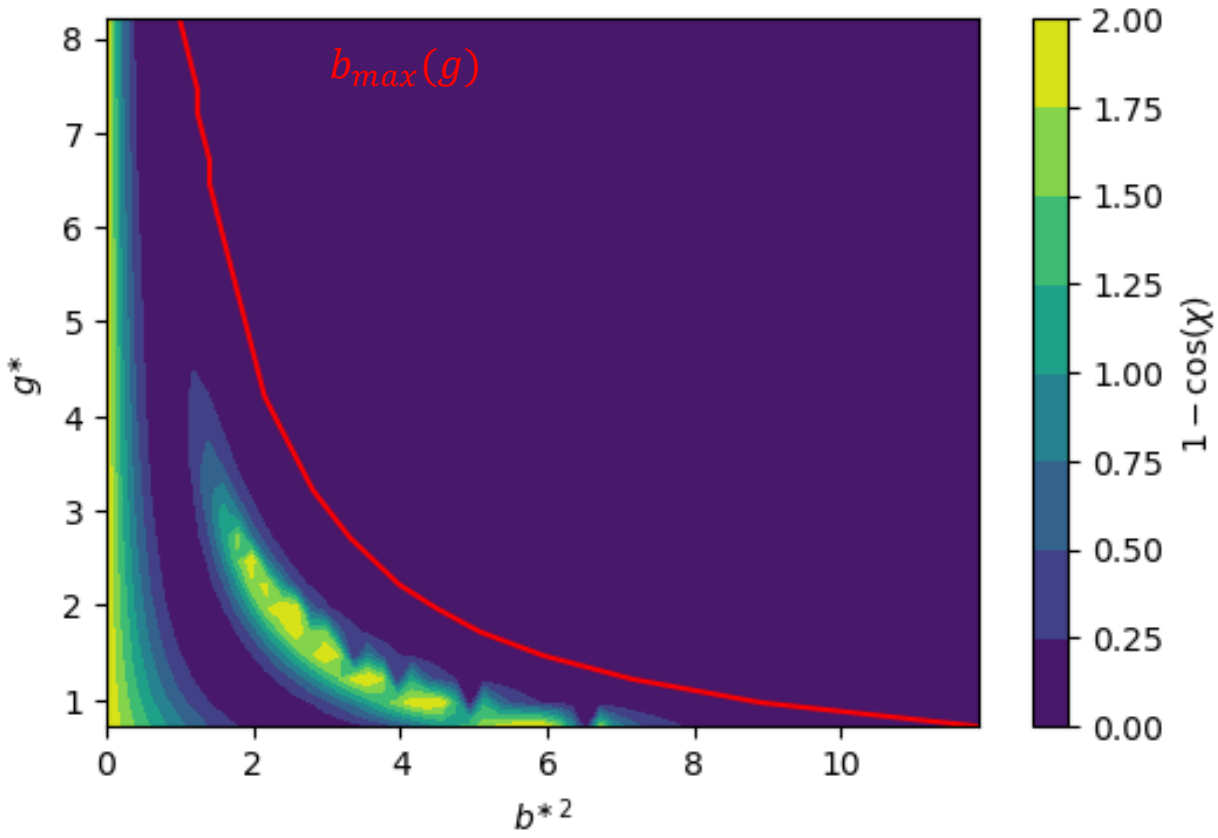

Figure S6-2. Contour plot of $1 - cos\,\chi$ (proportional to the momentum transfer) as a function of the impact parameter, b, and the relative velocity, g, of the colliding particles (both in dimensionless units). The red line denotes the threshold values $b_{max}(g)$ for every velocity point.

Section S6-3: Evaluating Collision Integrals using the Chapman-Enskog Formalism

The motion of ions through a gas is governed by the Boltzmann transport equation.[19] The quantity of interest in this framework is the ion velocity distribution, f_{ion}. One can calculate the drift velocity (v_D) as a moment of the ion velocity distribution (f_{ion}; Eq. S1), for which we use the convention that the electric field points along the z-axis. Note that n is a normalization factor.[20]

$$v_D = \langle v_z \rangle = \frac{1}{n} \int v_z f_{ion} \, dv \tag{S1}$$

Although the velocity distribution of the bath gas particles (f_{bg}) can be described by a Maxwell-Boltzmann distribution at temperature T, f_{ion} will be distorted compared to f_{bg} due to the acceleration caused by the electric field. Within the framework of 2TT, field-induced acceleration of the ion is accommodated by introducing a second temperature (T_{ion}) that accounts for the skewed velocity distribution. The effective temperature described in **Error! Reference source not found.** – **Error! Reference source not found.** reflects the distribution of *relative* velocities between bath gas particles and ions. In general, $T_{ion} \geq T_{eff} \geq T$. To solve for f_{ion}, one can apply the Chapman-Enskog formalism,[21,22] which expresses f_{ion} as a Taylor series of basis functions. 2TT expands on this formalism by using Burnett-like basis functions, which are defined in Eqs. S2 and S3:[23,24]

$$\psi_{lm}^{(r)}(w_{ion}) = w_{ion}^{l} S_{l+1/2}^{(r)}(w_{ion}^2)(Y_l^m(\theta, \phi)) \tag{S2}$$

$$w_{ion}^2 = \frac{mv^2}{2k_B(T_{ion})} \tag{S3}$$

Here, $S_{l+1/2}^{(r)}$ are Laguerre polynomials, Y_l^m are the spherical harmonics, m is the molecular mass of the ion, and v is its velocity. w_{ion} acts as dimensionless velocity to simplify the equations. Rather than

solving for the full ion velocity distribution, 2TT attempts to find solutions only to the moments of these basis functions. This is sufficient for ion mobility because the drift velocity can be expressed as moment of $\psi_{10}^{(0)}$, as per Eq. S4.

$$v_D = \sqrt{\frac{2k_B(T_{ion})}{m}} \left\langle \psi_{10}^{(0)} \right\rangle \tag{S4}$$

Iterative computation is used to solve for these moments, with higher-order approximations requiring additional iterations. The specifics of the iterative procedure are beyond the scope of this manuscript, although interested readers are directed to references 23 and 24 for further information.

Section S6-4: Velocity grid limits

To ensure that the integration over the relative velocity is accurate, limits for the velocity grid must be chosen such that the integrand, $Q^{(l)}\omega^{(s)}$, is significantly close to zero at those limits. Since it is not possible to predict the magnitude and functional dependency of $Q^{(l)}(g)$, we focused on the weight functions $\omega^{(s)}$. *I.e.*, we want to find velocity limits such that upon integration, the error caused by the cutoff becomes negligible. To simplify the algebra, we work with unitless velocity and temperature:

$$g^{*2} = \frac{\mu g^2}{2\epsilon'} \tag{S5a}$$

$$T^* = \frac{k_B T}{\epsilon'} \tag{S5b}$$

Here, μ is the reduced mass of the collision pair, k_B is the Boltzmann constant, and $\epsilon' = 1.34$ meV is a fixed energy constant.[1] Writing the weight functions now in dimensionless units:

$$\omega^{(s)}(g^*, T^*) = \left[\frac{(s+1)!}{2} T^{*s+2}\right]^{-1} \times g^{*2s+3} \exp\left(-\frac{g^{*2}}{T^*}\right) \tag{S6}$$

we can express their integrals as:

$$\int_0^{G_{upper}} \omega^{(s)}(g^*, T^*)\, \mathrm{d}g^* = 1 - \frac{1}{(s+1)!}\, \Gamma\left(s+2, \frac{G_{upper}^2}{T^*}\right) \tag{S7a}$$

$$\int_{G_{lower}}^{\infty} \omega^{(s)}(g^*, T^*)\,\mathrm{d}g^* = \frac{1}{(s+1)!}\ \Gamma\left(s+2, \frac{G_{lower}^2}{T^*}\right) \tag{S7b}$$

where Γ is the upper incomplete gamma function and G_{lower} and G_{upper} define the lower and upper limit for the velocity integration, respectively. From this, we can obtain and G_{lower} and G_{upper} by defining acceptable errors, *i.e.*, asking how close the integrals of Eq. (S7) should be to unity:

$$\frac{1}{(s+1)!}\ \Gamma\left(s+2, \frac{G_{upper}^2}{T^*}\right) = \xi_{upper} \tag{S8a}$$

$$\frac{1}{(s+1)!}\ \Gamma\left(s+2, \frac{G_{lower}^2}{T^*}\right) = 1 - \xi_{lower} \tag{S8b}$$

Because $Q^{(l)}(G_{lower}) \gg Q^{(l)}(G_{upper})$, we pick a tighter value for ξ_{lower}. However, a too low G_{lower} will result in lost trajectories because at very low relative velocities collision particles will stick to/orbit the ion. In the end, we chose:

$$\xi_{upper} = 10^{-3} \quad \overset{s=4}{\rightarrow} \quad G_{upper} = \sqrt{16.455 \cdot T_{upper}^*} \tag{S9a}$$

$$\xi_{lower} = 10^{-4} \quad \overset{s=1}{\rightarrow} \quad G_{lower} = \sqrt{0.0862 \cdot T_{lower}^*} \tag{S9b}$$

Here, T_{lower}^* is calculated from T_{bath} and T_{upper}^* is calculated from $T_{eff,max}$ according to Eq. (S1b).

Section S6-5: Avg-N2 versus CoM-N2 Potentials

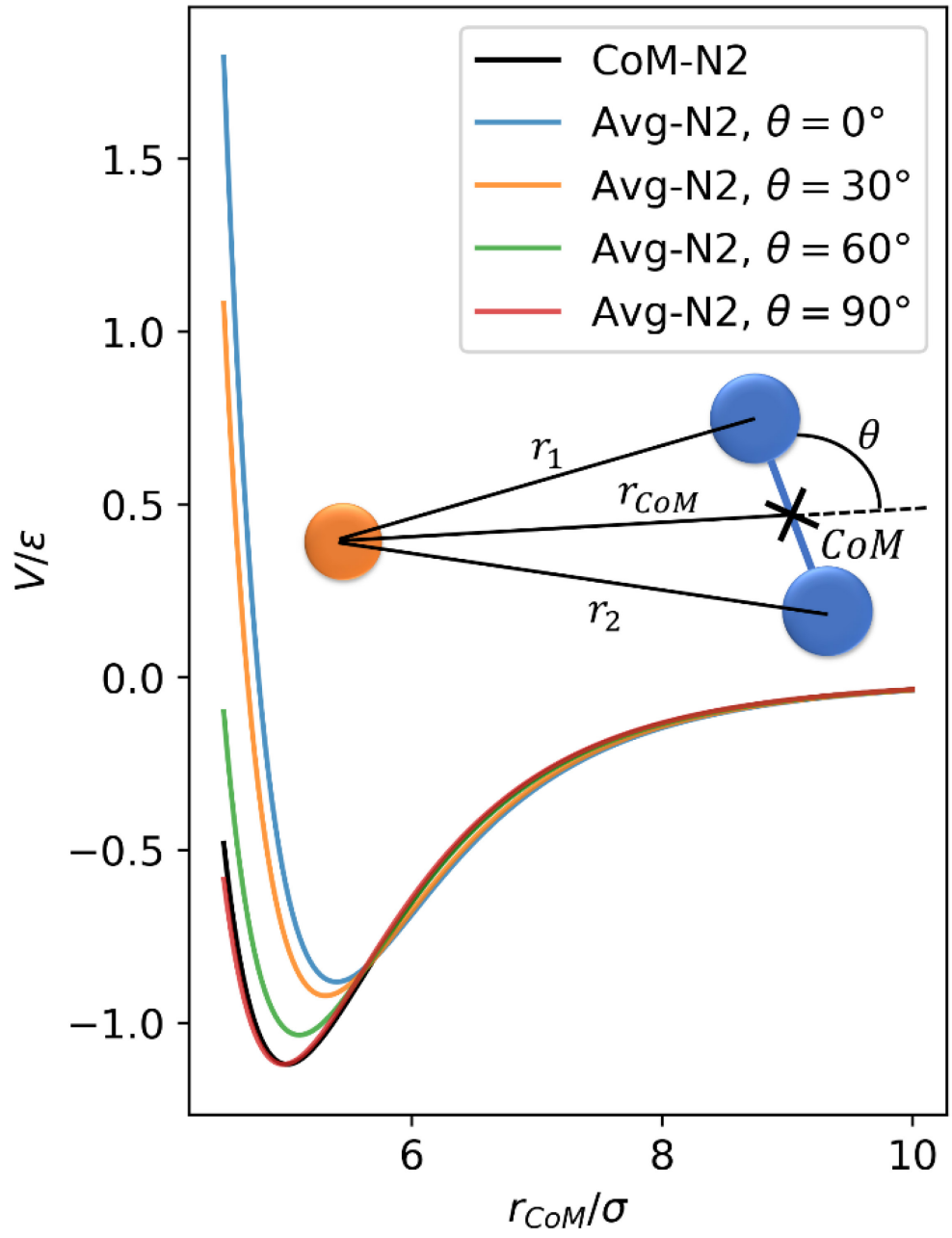

Figure S6-3. Van-der-Waals interaction potentials (Exp-6) for the CoM-N_2 and Avg-N_2 versions depending on the orientation of the N_2 molecule (described by the angle θ). While the CoM-N_2 potential is independent on θ, the Avg-N_2 potential shows a strong dependency. For a head-on collision ($\theta = 0°$), the potential becomes repulsive faster. This is more realistic because for a head-on collision, as one end of the N_2 molecule reaches the collision partner significantly earlier than its CoM.

Section S6-6: Precision for high-field calculations

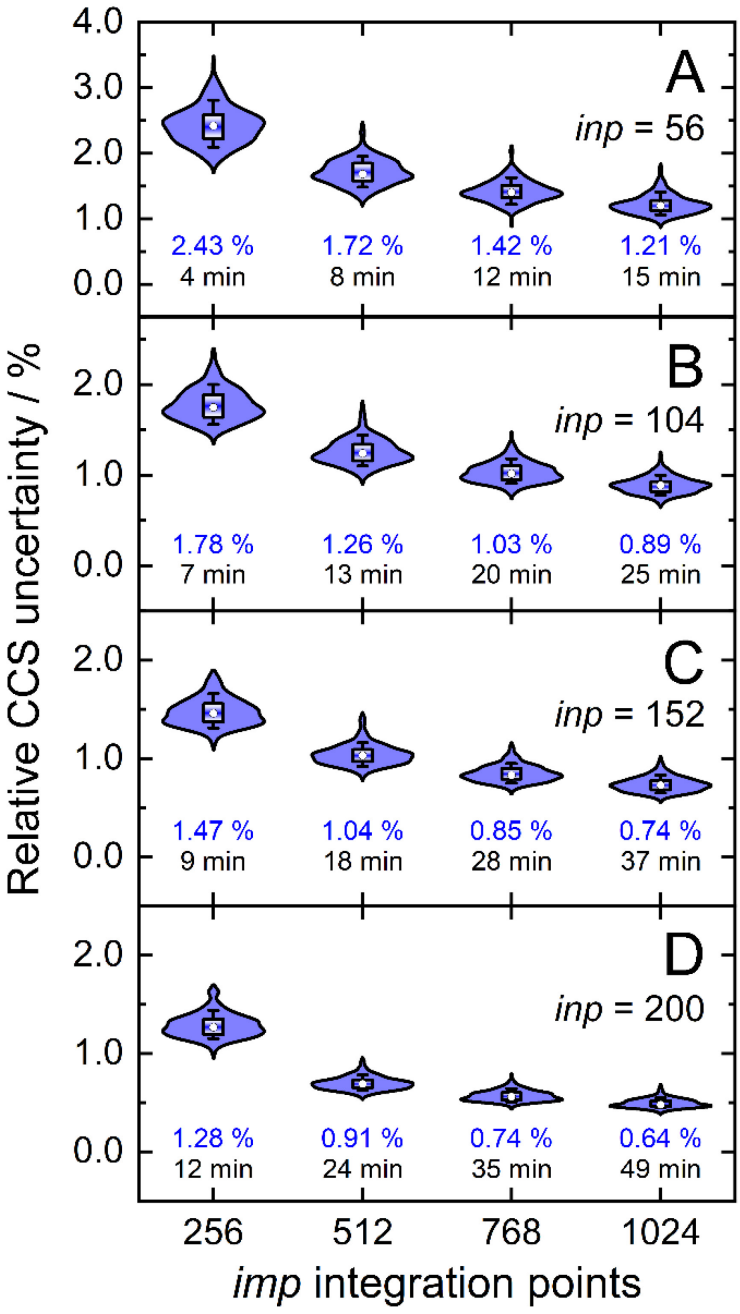

Figure S6-4. Distributions of relative CCS uncertainties, $\sigma_{CI}(\Omega^{(1,1)})/\Omega^{(1,1)}$, for the validation set ($N = 50$) for different combinations of velocity sample points (inp) and orientation/impact parameter sample points (imp) when calculating mobilities/CCS between 298 K and 800 K. Blue numbers below each distribution correspond to mean relative CCS uncertainties and black numbers to average computing time.

Section S6-7: Connection between alpha function and dispersion plot

The alpha function of an ion describes how the mobility at higher field strengths deviates from its value at infinitely small field strengths:

$$\alpha\left(\frac{E}{N}\right) = \frac{\left(K\left(\frac{E}{N}\right)\right)}{\left(K(0)\right)} - 1 \tag{S10}$$

In differential mobility spectrometry, to probe this alpha function, an asymmetric, oscillating field is applied containing both high- and low-field strengths. This separation field, $E_S(t)$ can have many forms (square wave, double sine, etc.)[25] but it is required that

$$\frac{1}{\tau}\int_0^\tau E_S(t)\ \mathrm{d}t = \langle E_S(t)\rangle = E_S\langle f(t)\rangle = 0 \tag{S11a}$$

$$\langle f^{2n+1}(t)\rangle \neq 0 \tag{S11b}$$

where $E_S(t) = E_S f(t)$ with $f(t)$ being the normalized form of the waveform and E_S its amplitude (maximum value). τ denotes the time for one wave cycle. Additional to the separation field, a constant field, E_C, is applied to ensure ion transmission. Thus, the total field is

$$E(t) = E_S f(t) + E_C \tag{S12}$$

A dispersion plot now measures the compensation field, E_C, ideal for ion transmission in dependence of the separation field amplitude, E_S. To obtain the alpha function from a measured dispersion plot,

Buryakov[26] suggested the following method: First, the dispersion plot data is fitted to an uneven polynomial of $(2N+1)$-th order:

$$E_C = \sum_{n=1}^{N} B_{2n+1} E_S^{2n+1} \tag{S13}$$

The obtained coefficients B_{2n+1} can then be used to determine the alpha function, expressed as even polynomial:[26,27]

$$\alpha(E) = \sum_{n=1}^{N} \alpha_{2n} E^{2n} \tag{S14a}$$

$$\alpha_{2n} = \frac{1}{\langle f^{2n+1}(t)\rangle}\left\{ B_{2n+1} + \sum_{k=1}^{n-1} (2(n-k)+1) B_{2k+1} \alpha_{2(n-k)} \langle f^{2(n-k)} \rangle \right\} \tag{S14b}$$

Note that this workflow can show deviations at the higher end of the field strengths, as is the case with every polynomial fitting. The lower end ($E \to 0$) is not an issue since the enforcement of $B_0 = \alpha_0 = 0$ ensures the correct behaviour, namely $E_C(E_S = 0) = 0$ and $\alpha(E = 0) = 0$. Conversely, the dispersion plot can also be predicted from knowing the alpha function. If E_C is expected to be very small as compared to E_S, Buryakov's first order approximation equation can be used:[26]

$$E_C = \frac{\langle \alpha f(t) \rangle E_S}{1 + \langle \alpha \rangle + \langle \alpha' f(t) \rangle E_S} \tag{S15}$$

Note, that $\alpha = \alpha\big(E_S(t)\big)$ but we omitted the field dependency for notational clarity. Further, $\alpha' = \mathrm{d}\alpha/\mathrm{d}E$. However, this equation breaks down if E_C becomes large as we recently showed in another

publication.[28] In this case, the compensation value, E_C, can be determined iteratively. *I.e.*, starting with a guess, $E_C^{(guess)}$, we calculate the net drift velocity of the ion caused by the asymmetry of the waveform according to

$$\langle v_D \rangle = \left\langle K \cdot [E_S f(t) + E_C^{(guess)}] \right\rangle \tag{S16}$$

Again, note that we omitted the explicit dependency of the mobility on the total separation field, $K = K\big(E(t)\big) = K(E_S f(t) + E_C)$. The mobility can be obtained from the alpha function by rearranging Eq. (S8). We then use the obtained net drift velocity to obtain a new guess for the separation field as

$$E_C^{(new)} = E_C^{(old)} - \frac{\langle v_D \rangle}{K(0)} \delta_{damp} \tag{S17}$$

where δ_{damp} is a damping factor usually used in iterative procedures. The new guess of E_C is used again in Eq. (S14) and this procedure is repeated until $\langle v_D \rangle < v_{thresh}$, *i.e.*, until the drift velocity left is negligible.

Section S6-8: Details concerning the empirical correction to 2TT

S6-8.1: Choice of functional form

Siems *et al.*[29] compared 2nd order 2TT with accurate modelling of an ion's mobility using the Gram-Charlier (GC) approach for idealized test systems, *i.e.*, atomic ions in atomic gases. They found that 2TT yields good results over a broad range of field strength (0-50 Td) but shows 5-7% deviations above 100 Td. For the "heavy ion" case, *i.e.*, when the ion is much heavier than the bath gas particle, the deviations are zero at low fields, then the 2TT mobilities become increasingly too small, eventually reaching a constant underestimation at very high field strengths. To correct for this deviation, we should pick a form that matches this behaviour: no deviations at low fields, constant deviation at very high fields and a smooth transition in between. Thus, we chose

$$K_{corr} = f_{corr} \cdot K_{2TT} \tag{S18a}$$

$$f_{corr}\left(\frac{E}{N}\right) = 1 + A \exp\left(-\frac{B}{E/N}\right) \tag{S18b}$$

As can be seen in Figure S6-5, the form of f_{corr} fulfills these requirements. At low fields $f_{corr} = 1$ so that $K_{corr} = K_{2TT}$. Increasing the field strength leads to an increase in f_{corr} up to a fixed correction of $K_{corr} = (1 + A)K_{2TT}$ in the limit of very high E/N, corresponding to a relative increase of the mobility by A (%). How fast we switch from $f_{corr} = 1$ to $f_{corr} = 1 + A$ is determined by B.

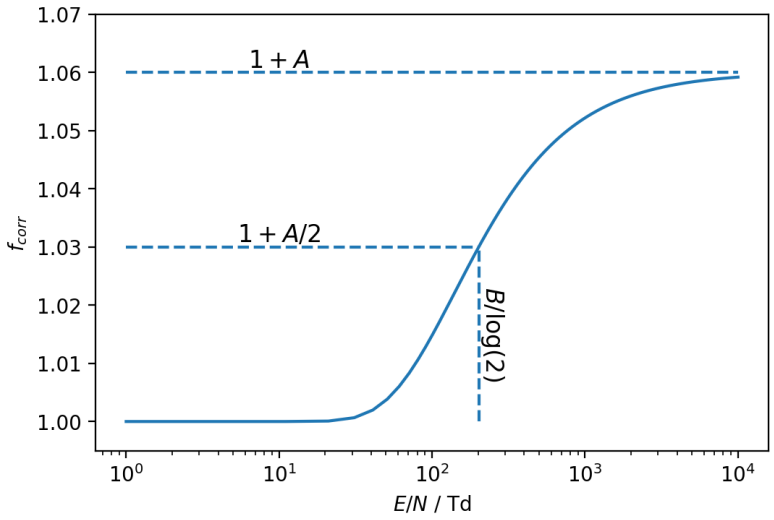

Figure S6-5. Functional form of the empirical correction used here. The parameters A and B determine the limit at very high fields and the speed of the rise, respectively. Here, we used representative values of $A = 6$ % and $B = 140$ Td.

Further justification of the functional form chosen comes from comparison of the difference between measured and predicted alpha function of protonated amoxapine (see Fig. 6A of the main manuscript). Given multiplicative nature of our correction, we can obtain the needed correction from the experimental and 2TT predicted alpha function according to

$$f_{true} = \frac{\alpha_{expt} + 1}{\alpha_{2TT} + 1} \tag{S19}$$

S6-8.2: Examples of dispersion plots utilizing the empirical correction

Calculated mobilities within 2nd order 2TT (K_{2TT}) were used to model dispersion plot behavior of the 132 compounds in the "high-field validation set" according to the method (see Section S6-7). In general, we find that 2TT overestimates the measured dispersion plots, which is in line with the deviations found by Siems *et al.* To study the extent in which K_{2TT} needs to be corrected, we fit the parameters A and B for all 132 compounds such that the experimental dispersion plots were predicted most accurately. The average over all parameters A and B were then used as common empirical correction.

The results of this procedure can be seen in Figure S6-6 for two examples. As mentioned in Chapter 6.11, the uncorrected 2TT overshoots the measured dispersion plots. Individual fitting of the empirical correction, however, yields dispersion plots that are very well within the experimental uncertainties. This gives us confidence that the functional form chosen is well suited for this task. Finally, Figure S6- shows the calculated dispersion plots utilizing the fixed empirical correction (A_{avg}, B_{avg}). In case of Bentazon, this still yields very good agreement with the experimental data since the individually fitted empirical correction parameters are almost identical to the averaged ones. In contrast, the fixed empirical correction shows larger deviations to the experimental data as compared to the individually fitted ones. This can also be seen by comparing the correction parameters, which are rather different for the individually and fixed empirical correction. Specifically, the fixed empirical correction if too large and thus corrects the mobilities more than needed. Nevertheless, we would argue that the dispersion plot with (fixed) empirical correction resembles the experimental one better or at least as good as the uncorrected 2TT predicted one.

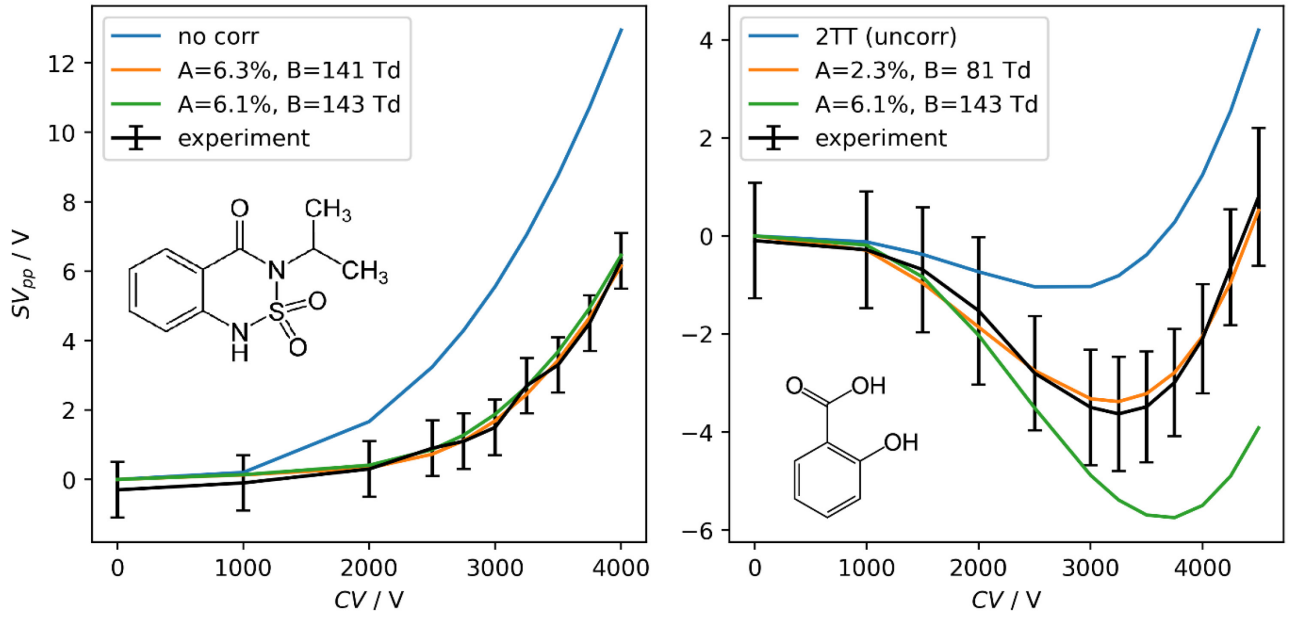

Figure S6-6. Measured and calculated dispersion plots of Bentazon (**left**) and Salicylic Acid (**right**). Calculated dispersion plots are shown for uncorrected 2[nd] order 2TT, for 2TT with individually fitted empirical correction, and for 2TT with the fixed empirical correction utilizing $A_{avg} = 6.1$ % and $B_{avg} = 143$ Td.

S6-8.3: Correlation of A and B fit parameters to physicochemical properties

Prior to using the average of the distributions of A and B, i.e., A_{avg} and B_{avg}, we attempted to correlate the optimized A and B parameters to properties relevant to the simulation of collision dynamics. However, no significant correlation between any of the selected quantities was found (Figure S6-7).

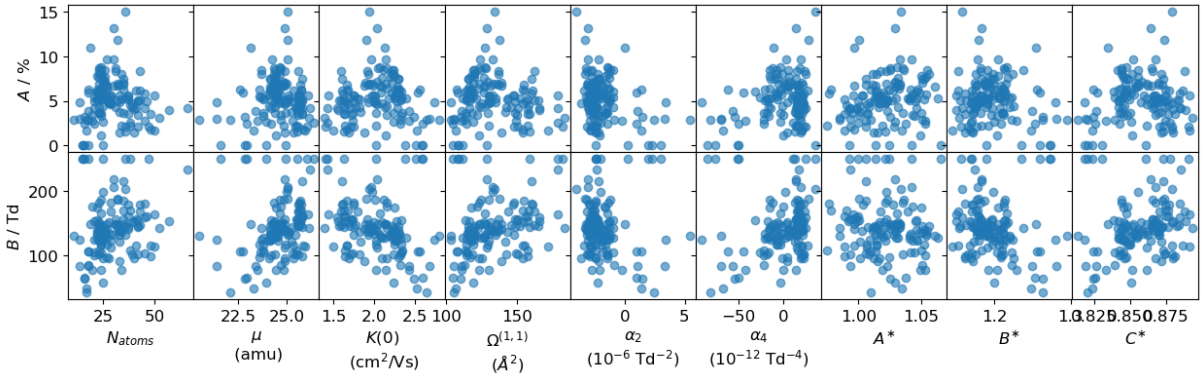

Figure S6-7. Correlation between the A and B parameters to typical parameters appearing in the formalism of ion mobility, namely the number of atoms (N_{atoms}), the reduced mass (μ), the low field mobility ($K(0)$), the first collision integral ($\Omega^{(1,1)}$), alpha function coefficients (α_2 and α_4) and important ratios of collision integrals ($A^* = \Omega^{(2,2)}/\Omega^{(1,1)}$, $B^* = (5\Omega^{(1,2)} - 4\Omega^{(1,3)})/\Omega^{(1,1)}$, and $C^* = \Omega^{(1,2)}/\Omega^{(1,1)}$).

Section S6-9: Additional plots from benchmarking MobCal-MPI 2.0

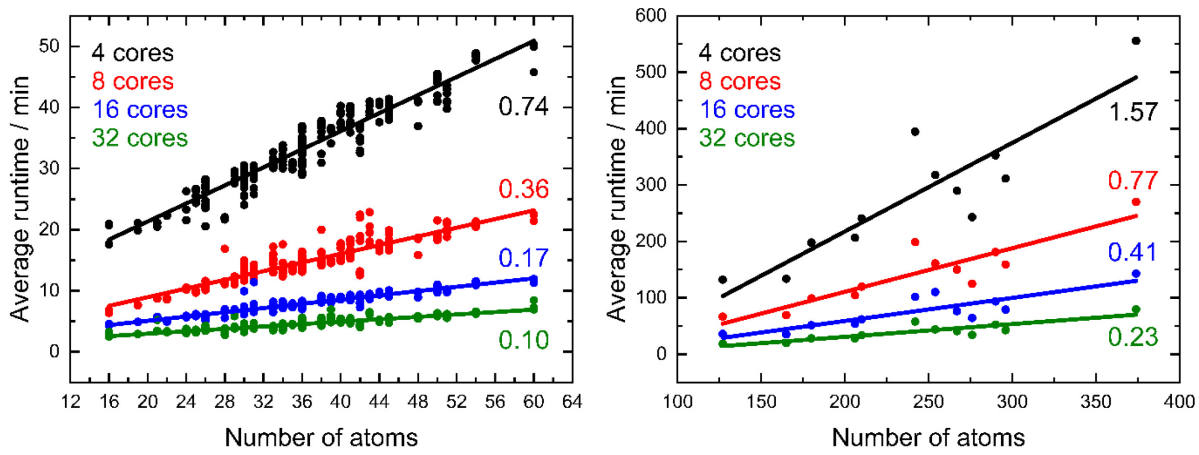

Figure S6-8. Benchmarking of runtimes to calculate CCSs in dependence of the number of cores used in parallel computing. Slopes corresponding to linear regression of the benchmarking data are shown on the right side of each figure. **(Left):** Test data is composed of the 238 different conformers of the validation set. **(Right):** Test data is composed of 12 peptides from the peptide set. All calculations are repeated for three different random seed numbers. The linear behavior shows the expected $\mathcal{O}(N)$ dependency with respect to the number of atoms, whereas the $1/N_{cores}$ decrease in the slopes (numbers adjacent to the regressions) indicates efficient parallelization.

References

(1) Mesleh, M. F.; Hunter, J. M.; Shvartsburg, A. A.; Schatz, G. C.; Jarrold, M. F. Structural Information from Ion Mobility Measurements: Effects of the Long-Range Potential. *J Phys Chem* **1996**, *100* (40), 16082–16086. https://doi.org/10.1021/jp961623v.

(2) Shvartsburg, A. A.; Jarrold, M. F. An Exact Hard-Spheres Scattering Model for the Mobilities of Polyatomic Ions. *Chem Phys Lett* **1996**, *261* (1–2), 86–91. https://doi.org/10.1016/0009-2614(96)00941-4.

(3) Kim, H.; Kim, H. I.; Johnson, P. V.; Beegle, L. W.; Beauchamp, J. L.; Goddard, W. A.; Kanik, I. Experimental and Theoretical Investigation into the Correlation between Mass and Ion Mobility for Choline and Other Ammonium Cations in N 2. *Anal Chem* **2008**, *80* (6), 1928–1936. https://doi.org/10.1021/ac701888e.

(4) Campuzano, I.; Bush, M. F.; Robinson, C. V.; Beaumont, C.; Richardson, K.; Kim, H.; Kim, H. I. Structural Characterization of Drug-like Compounds by Ion Mobility Mass Spectrometry: Comparison of Theoretical and Experimentally Derived Nitrogen Collision Cross Sections. *Anal Chem* **2012**, *84* (2), 1026–1033. https://doi.org/10.1021/ac202625t.

(5) Lee, J. W.; Davidson, K. L.; Bush, M. F.; Kim, H. I. Collision Cross Sections and Ion Structures: Development of a General Calculation Method via High-Quality Ion Mobility Measurements and Theoretical Modeling. *Analyst* **2017**, *142* (22), 4289–4298. https://doi.org/10.1039/C7AN01276D.

(6) Lee, J. W.; Lee, H. H. L.; Davidson, K. L.; Bush, M. F.; Kim, H. I. Structural Characterization of Small Molecular Ions by Ion Mobility Mass Spectrometry in Nitrogen Drift Gas: Improving the Accuracy of Trajectory Method Calculations. *Analyst* **2018**, *143* (8), 1786–1796. https://doi.org/10.1039/C8AN00270C.

(7) Ieritano, C.; Crouse, J.; Campbell, J. L.; Hopkins, W. S. A Parallelized Molecular Collision Cross Section Package with Optimized Accuracy and Efficiency. *Analyst* **2019**, *144* (5), 1660–1670. https://doi.org/10.1039/C8AN02150C.

(8) Ieritano, C.; Hopkins, W. S. Assessing Collision Cross Section Calculations Using MobCal-MPI with a Variety of Commonly Used Computational Methods. *Mater Today Commun* **2021**, *27* (February), 102226. https://doi.org/10.1016/j.mtcomm.2021.102226.

(9) Zanotto, L.; Heerdt, G.; Souza, P. C. T.; Araujo, G.; Skaf, M. S. High Performance Collision Cross Section Calculation-HPCCS. *J Comput Chem* **2018**, *39* (21), 1675–1681. https://doi.org/10.1002/jcc.25199.

(10) Larriba, C.; Hogan, C. J. Free Molecular Collision Cross Section Calculation Methods for Nanoparticles and Complex Ions with Energy Accommodation. *J Comput Phys* **2013**, *251*, 344–363. https://doi.org/10.1016/j.jcp.2013.05.038.

(11) Larriba, C.; Hogan, C. J. Ion Mobilities in Diatomic Gases: Measurement versus Prediction with Non-Specular Scattering Models. *J Phys Chem A* **2013**, *117* (19), 3887–3901. https://doi.org/10.1021/jp312432z.

(12) Larriba-Andaluz, C.; Fernández-García, J.; Ewing, M. A.; Hogan, C. J.; Clemmer, D. E. Gas Molecule Scattering & Ion Mobility Measurements for Organic Macro-Ions in He versus N 2 Environments. *Physical Chemistry Chemical Physics* **2015**, *17* (22), 15019–15029. https://doi.org/10.1039/C5CP01017A.

(13) Shrivastav, V.; Nahin, M.; Hogan, C. J.; Larriba-Andaluz, C. Benchmark Comparison for a Multi-Processing Ion Mobility Calculator in the Free Molecular Regime. *J Am Soc Mass Spectrom* **2017**, *28* (8), 1540–1551. https://doi.org/10.1007/s13361-017-1661-8.

(14) Ewing, S. A.; Donor, M. T.; Wilson, J. W.; Prell, J. S. Collidoscope: An Improved Tool for Computing Collisional Cross-Sections with the Trajectory Method. *J Am Soc Mass Spectrom* **2017**, *28* (4), 587–596. https://doi.org/10.1007/s13361-017-1594-2.

(15) Bleiholder, C.; Wyttenbach, T.; Bowers, M. T. A Novel Projection Approximation Algorithm for the Fast and Accurate Computation of Molecular Collision Cross Sections (I). Method. *Int J Mass Spectrom* **2011**, *308* (1), 1–10. https://doi.org/10.1016/j.ijms.2011.06.014.

(16) Bleiholder, C.; Contreras, S.; Do, T. D.; Bowers, M. T. A Novel Projection Approximation Algorithm for the Fast and Accurate Computation of Molecular Collision Cross Sections (II). Model Parameterization and Definition of Empirical Shape Factors for Proteins. *Int J Mass Spectrom* **2013**, *345–347*, 89–96. https://doi.org/10.1016/j.ijms.2012.08.027.

(17) Anderson, S. E.; Bleiholder, C.; Brocker, E. R.; Stang, P. J.; Bowers, M. T. A Novel Projection Approximation Algorithm for the Fast and Accurate Computation of Molecular Collision Cross Sections (III): Application to Supramolecular Coordination-Driven Assemblies with Complex Shapes. *Int J Mass Spectrom* **2012**, *330–332*, 78–84. https://doi.org/10.1016/j.ijms.2012.08.024.

(18) Bleiholder, C.; Contreras, S.; Bowers, M. T. A Novel Projection Approximation Algorithm for the Fast and Accurate Computation of Molecular Collision Cross Sections (IV). Application to Polypeptides. *Int J Mass Spectrom* **2013**, *354–355*, 275–280. https://doi.org/10.1016/j.ijms.2013.06.011.

(19) Boltzmann, L. Weitere Studien Über Das Wärmegleichgewicht Unter Gasmolekülen. *Sitzungsberichte der kaiserlichen Akademie der Wissenschaften (II)* **1872**, *66*, 275–370.

(20) Mason, E. A.; McDaniel, E. W. *Transport Properties of Ions in Gases*; John Wiley and Sons: New York, 1988.

(21) Chapman, S.; Cowling, T. G. *The Mathematical Theory of Non-Uniform Gases*, 3rd ed.; Cambridge University Press: London, UK, 1970.

(22) Hirschfelder, J. O.; Curtiss, C. F.; Bird, R. B. *Molecular Theory of Gases and Liquids*, Corrected.; John Wiley \& Sons, Inc.: New York, NY, USA, 1964.

(23) Viehland, L. A.; Mason, E. A. Gaseous Lon Mobility in Electric Fields of Arbitrary Strength. *Ann Phys (N Y)* **1975**, *91* (2), 499–533. https://doi.org/10.1016/0003-4916(75)90233-X.

(24) Viehland, L. A.; Mason, E. A. Gaseous Ion Mobility and Diffusion in Electric Fields of Arbitrary Strength. *Ann Phys (N Y)* **1978**, *110* (2), 287–328. https://doi.org/10.1016/0003-4916(78)90034-9.

(25) Krylov, E. V; Coy, S. L.; Vandermey, J.; Schneider, B. B.; Covey, T. R.; Nazarov, E. G. Selection and Generation of Waveforms for Differential Mobility Spectrometry. *Rev Sci Instrum* **2010**, *81* (2), 024101. https://doi.org/10.1063/1.3284507.

(26) Buryakov, I. A.; Krylov, E. V.; Nazarov, E. G.; Rasulev, U. K. A New Method of Separation of Multi-Atomic Ions by Mobility at Atmospheric Pressure Using a High-Frequency Amplitude-Asymmetric Strong Electric Field. *Int J Mass Spectrom Ion Process* **1993**, *128* (3), 143–148. https://doi.org/10.1016/0168-1176(93)87062-W.

(27) Krylov, E.; Nazarov, E. G.; Miller, R. A.; Tadjikov, B.; Eiceman, G. A. Field Dependence of Mobilities for Gas-Phase-Protonated Monomers and Proton-Bound Dimers of Ketones by Planar Field Asymmetric Waveform Ion Mobility Spectrometer (PFAIMS). *J Phys Chem A* **2002**, *106* (22), 5437–5444. https://doi.org/10.1021/jp020009i.

(28) Haack, A.; Hopkins, W. S. Kinetics in DMS: Modeling Clustering and Declustering Reactions. *J Am Soc Mass Spectrom* **2022**, *33* (12), 2250–2262. https://doi.org/10.1021/jasms.2c00224.

(29) Siems, W. F.; Viehland, L. A.; Hill, H. H. Correcting the Fundamental Ion Mobility Equation for Field Effects. *Analyst* **2016**, *141* (23), 6396–6407. https://doi.org/10.1039/C6AN01353H.